The Community Stress-Drop Validation Study—Part II: Uncertainties of the Source Parameters and Stress Drop Analysis

Dino Bindi[*1], Daniele Spallarossa[2], Matteo Picozzi[3], Adrien Oth[4], Paola Morasca[5], and Kevin Mayeda[6]

Abstract

As part of the community stress-drop validation study, we evaluate the uncertainties of seismic moment M_0 and corner frequency f_c for earthquakes of the 2019 Ridgecrest sequence. Source spectra were obtained in the companion article by applying the spectral decomposition approach with alternative processing and model assumptions. The objective of the present study is twofold: first, to quantify the impact of different assumptions on the source parameters; and second, to use the distribution of values obtained with different assumptions to estimate an epistemic contribution to the uncertainties. Regarding the first objective, we find that the choice of the attenuation model has a strong impact on f_c results: by introducing a depth-dependent attenuation model, f_c estimates of events shallower than 6 km increase of about 10%. Also, the duration of the window used to compute the Fourier spectra show an impact on f_c: the average ratio between the estimates for 20 s duration to those for 5 s decreases from 1.1 for $M_w < 3$ to 0.66 for $M_w > 4.5$. For the second objective, we use a mixed-effect regression to partition the intraevent variability into duration, propagation, and site contributions. The standard deviation ϕ of the intraevent residuals for $\log(f_c)$ is 0.0635, corresponding to a corner frequency ratio $10^{2\phi} = 1.33$. When the intraevent variability is compared to uncertainties on $\log(f_c)$, we observe that 2ϕ is generally larger than the 95% confidence interval of $\log(f_c)$, suggesting that the uncertainty of the source parameters provided by the fitting procedure might underestimate the model-related (epistemic) uncertainty. Finally, although we observe an increase of $\log(\Delta\sigma)$ with $\log(M_0)$ regardless of the model assumptions, the increase of $\Delta\sigma$ with depth depends on the assumptions, and no significant trends are detected when depth-dependent attenuation and velocity values are considered.

Cite this article as Bindi, D., D. Spallarossa, M. Picozzi, A. Oth, P. Morasca, and K. Mayeda (2023). The Community Stress-Drop Validation Study —Part II: Uncertainties of the Source Parameters and Stress Drop Analysis, *Seismol. Res. Lett.* **94**, 1992–2002, doi: 10.1785/0220230020.

Supplemental Material

Introduction

Source parameters, such as seismic moment and corner frequency, are generally computed from far-field measurements after making corrections for propagation and site effects. Because of the nonuniqueness of the decomposition into source, propagation, and site effects, the applied processing and model assumptions make it difficult to compare the results provided by different studies (Shearer *et al.*, 2019; Abercrombie, 2021; Pennington *et al.*, 2021). In addition, the availability of information only over a limited bandwidth and the strong near-surface attenuation effects limit our ability to retrieve the source parameters, in particular for small magnitude events (e.g., Bindi *et al.*, 2020; Chen and Abercrombie, 2020). In the companion article (see Data and Resources), we analyzed seismic recordings of the 2019 Ridgecrest sequence distributed as part of the community stress-drop validation study (Baltay *et al.*, 2021). We applied a spectral decomposition approach (Andrews, 1986) to produce a data set of source spectra in which, for each event, multiple solutions associated with different model assumptions are available. In this study, we compare the different solutions arranged in a logic-tree structure with the aim of capturing the systematic effects of the

1. German Research Centre for Geoscience GFZ, Potsdam, Germany, https://orcid.org/0000-0002-8619-2220 (DB); 2. Department for Earth, Environment, and Life Sciences DISTAV, University of Genova, Genova, Italy, https://orcid.org/0000-0002-8021-3908 (DS); 3. Department of Physics, University of Naples Federico II, Naples, Italy, https://orcid.org/0000-0001-8078-9416 (MP); 4. European Center for Geodynamics and Seismology, Walferdange, Grand-Duchy of Luxembourg, https://orcid.org/0000-0003-4859-6504 (AO); 5. National Institute of Geophysics and Volcanology INGV, Milan, Italy, https://orcid.org/0000-0002-6525-4867 (PM); 6. Air Force Technical Applications Center AFTAC, Florida, U.S.A., https://orcid.org/0000-0003-0980-0605 (KM)

*Corresponding author: bindi@gfz-potsdam.de

different processing and model assumptions. Through a random-effect analysis, we also quantify the intraevent variability that we compare with the confidence intervals (CIs) estimated for the source parameters. Even in the limited number of cases analyzed, we find that for most events the variability between the different branches of the logic tree is larger than the uncertainty provided as CIs of the source parameter estimates. This result implies that the precision of source parameters estimated without considering the epistemic component could lead to an overstimation of the accuracy of the source parameters. In addition, considering the entire population of earthquakes analyzed (about 500 events), we use Sammon maps (Sammon, 1969) to reduce the dimension of the vector measuring the similarity between the source spectra predicted by the models associated with the different branches of the logic tree. Analysis of Sammon's maps allows us to visualize the systematic impacts that the different assumptions considered have on source spectra predicted using the computed source parameters.

Logic Tree

In the companion article (see Data and Resources), hereinafter referred to as part I, we described the generalized inversion technique (GIT) decomposition applied to the Ridgecrest benchmark data set. Through the GIT decomposition, a single nonparametric source spectrum was obtained for each earthquake. Because data processing is described in part I, here we only recall that we considered 556 earthquakes recorded at 67 sites (corresponding to 94 stations if co-located sensors are counted separately). We analyzed both accelerometric (i.e., HN and HL) and velocimetric (i.e., HH and EH) channels with a sampling rate above 80 Hz, and Fourier amplitude spectra (FAS) computed for the two horizontal components were vectorially summed. In part I, we considered alternative choices for processing and model components: three different durations for FAS calculation, that is, 5 s, 20 s, and a variable duration between 5 and 20 s depending on the cumulative squared velocity; two different attenuation models based the first on hypocentral distance (HYPO model) and the second on epicentral distance for different depth intervals (EPIH model); two alternative site reference conditions in which the average site amplification is constrained to 1 regardless of the frequency (AVE amplification constraint), or the average amplification for a group of stations is constrained to an a priori selected amplification function (SEL amplification constraint). As discussed in part I, because the AVE amplification constraint shifts to sources an average near-surface attenuation common to all stations, the nonparametric source spectra obtained from AVE are fitted with a modified Brune model. The modification consists of multiplying the standard Brune spectrum with an exponential term (see equation 7 in part I) controlled by the parameter k_s. Therefore, a difference between the final results of the AVE and SEL branches is also given by a different tradeoff structure between the source parameters.

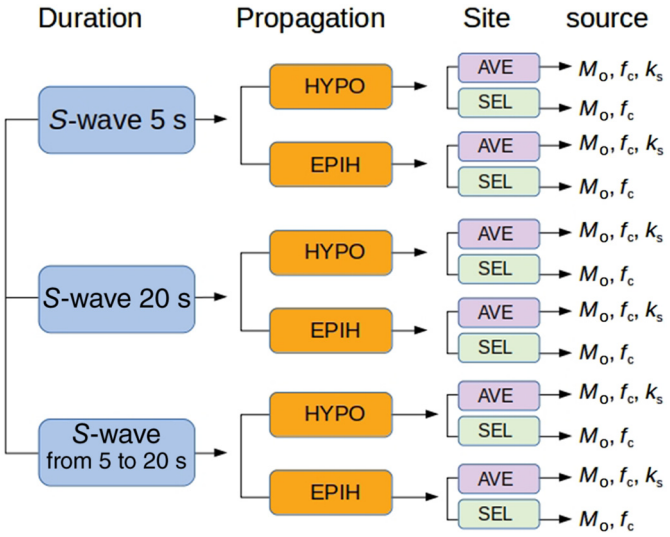

Figure 1. Logic-tree structure of alternative model assumptions applied to generalized inversion technique (GIT). The first level of branching relates to the window duration used for Fourier amplitude spectra (FAS) calculation (5 s, 20 s, and variable length); the second level of branching relates to the attenuation model (the hypocentral distance-based model and the depth-dependent models for epicentral distance are denoted with HYPO and EPIH, respectively); the third level of branching relates to the applied reference site constraint (i.e., constrained average of all stations and constrained average of a group of stations are indicated with average site amplification [AVE] and selected amplification function [SEL], respectively) along with the corresponding source model (Brune model and modified Brune model that takes into account the high-frequency decay of the acceleration spectrum as quantified by the k_s parameter). For details of the implemented decisions and models, see the companion article (Data and Resources). The color version of this figure is available only in the electronic edition.

In this work, the alternative choices are organized in a logic-tree structure (Fig. 1), and the GIT inversion performed for all branches formed by the combination of all choices (12 branches in total) are compared. The results in terms of source parameters are shown in Figures 2–4. Each figure shows the results for the seismic moment in Figures 2a,b, 3a,b, and 4a,b and for corner frequency in Figures 2c,d, 3c,d, and 4c,d; Figures 2a,c, 3a,c, and 4a,c show one-to-one comparisons for the alternative choices, and in Figures 2b,d, 3b,d, and 4b,d, the results are shown in terms of ratios with respect to a particular choice used as a reference.

Figure 2 compares the results obtained for two duration windows, that is, 5 and 20 s, considering the branches for EPIH attenuation and SEL site constraint. Seismic moments show small deviations (not exceeding 5%) with the tendency for longer duration to produce higher seismic moments for magnitudes above 4.5. More pronounced differences are

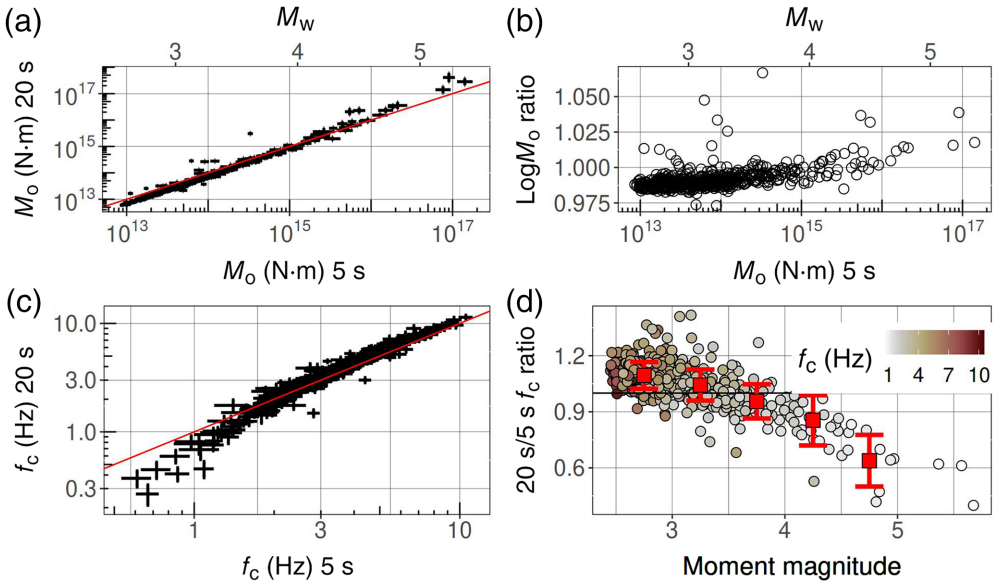

Figure 2. (a,b) Seismic moment M_0 and (c,d) corner frequency f_c obtained considering 5 and 20 s duration windows, EPIH attenuation model, and SEL site amplification constraint. The ratios in panels (b) and (d) are computed as values obtained for 20 s divided by values obtained for 5 s. The color version of this figure is available only in the electronic edition.

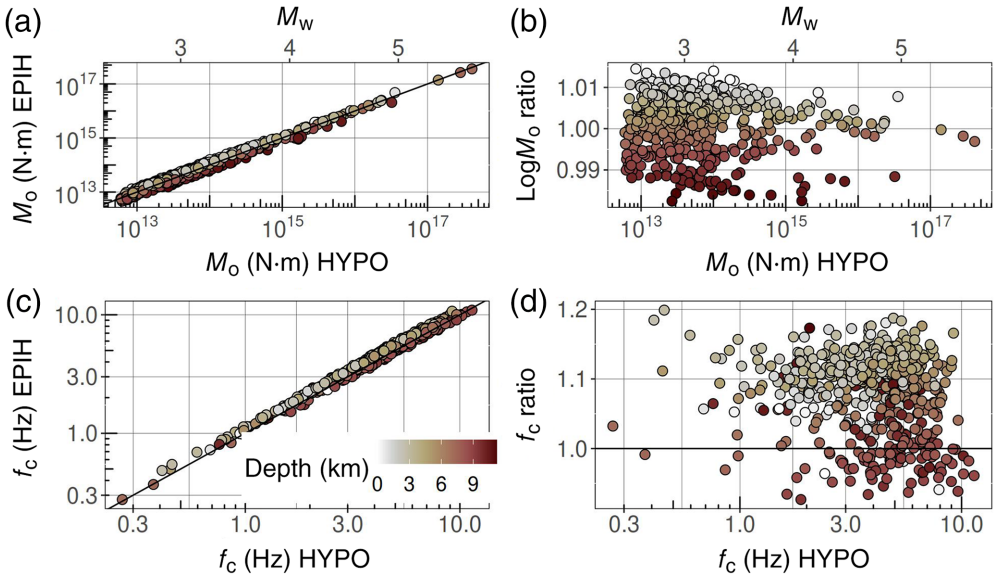

Figure 3. (a,b) Seismic moment M_0 and (c,d) corner frequency f_c obtained considering EPIH and HYPO attenuation models, 20 s duration windows, and SEL site amplification constraint. The ratios in panels (b) and (d) are computed as values obtained for EPIH divided by values obtained for HYPO. The color version of this figure is available only in the electronic edition.

observed for corner frequencies. Figure 2d shows that a systematic trend for the ratio between the f_c estimates for 20 s and 5 s duration develops with magnitude. For magnitudes smaller than 3, the 20 s duration produces f_c on average 10% larger than the 5 s duration. Then, the average ratio decreases with increasing magnitude and for magnitude above 4.5, the average ratio is 0.64. When the variable duration is considered (see Fig. S1, available in the supplemental material to this article), the estimated f_c values for magnitudes smaller than about 4 are consistent with those obtained considering 5 s; for larger magnitudes, an average reduction of about 10% is observed. We interpret this feature as a consequence of the limited resolution at low frequencies for spectra computed considering a duration of 5 s. Similar conclusions are drawn by considering other branches.

Figure 3 compares the results obtained for the two attenuation models, considering the branches for the 20 s windows and the SEL site constraint (similar results are obtained considering the other durations). Figure 3a,c shows that the results are consistent and, as expected from the role played by hypocentral depth in the two attenuation models, the differences are controlled by depth (used to fill in the symbols). The systematic dependency on depth is observed for both seismic moment and corner frequency, but stronger for the latter. Differences in the logarithm of seismic moments are systematic with depth (Fig. 3b), but within 2%; for the corner frequencies (Fig. 3d), EPIH model produces higher corner frequencies, particularly for depths shallower than 6 km, for which the average ratio is 1.1. For depths deeper than 6 km, the average ratio is 1.02. We ascribe this feature to a relative underestimation of the HYPO attenuation for shallow events with respect to EPIH.

Figure 4 compares the results obtained for the AVE and SEL site constraints, considering the branches for the 20 s window and the EPIH attenuation model (similar results are obtained considering the other durations). The alternative but reasonable choices produce consistent one-to-one scaling (Fig. 4a,c) but with differences controlled by specific parameters. For the case in Figure 4, the source parameter ratios scale with k_s and, similarly to the previous cases, the scaling is stronger for the corner frequency. Figure 4d shows that strong near-source attenuation (i.e., high-frequency slopes significantly larger than 2) corresponds to a corner frequency ratio less than 0.8. We interpret this feature as due to the inverse correlation existing between the corner frequency and k_s, as quantified by the covariance matrix (here not shown).

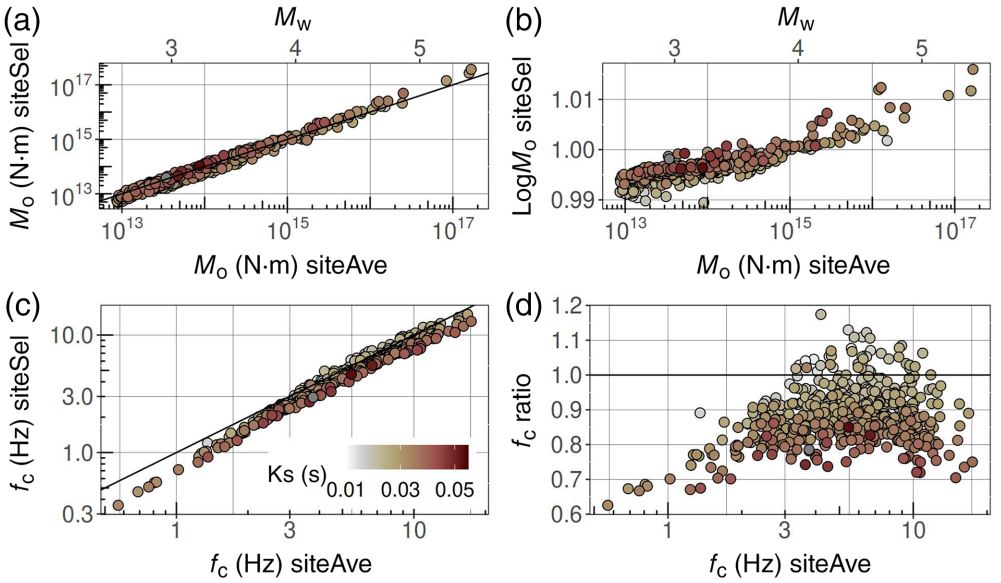

Figure 4. (a,b) Seismic moment M_0 and (c,d) corner frequency f_c obtained considering SEL and AVE site amplification constraints, EPIH attenuation model, and 20 s window duration. The ratios in panels (b) and (d) are computed as SEL results over AVE. The symbols are filled according to the k_s values associated with AVE results. The color version of this figure is available only in the electronic edition.

Model-Related Uncertainties

We quantify the systematic (i.e., repeated) effects on source parameters generated by the assumptions on duration, attenuation, and site constraints described in the Logic Tree section. In the following, we focus on the corner frequency f_c that has been shown to be more affected than the seismic moment. Our approach is to consider duration, attenuation, and site constraint as grouping factors and to partition the overall distribution of residuals into different components using a mixed effects regression (Atik *et al.*, 2010; Stafford, 2014; Bates *et al.*, 2015). The regression model is the following:

$$\log(f_c) = e_1 + \eta_{\text{event}} + \eta_{\text{duration}} + \eta_{\text{propagation}} + \eta_{\text{site}} + \epsilon, \quad (1)$$

in which $\log(f_c)$ is including the corner frequencies of all events as estimated by the different branches of the logic tree; e_1 is the intercept (or offset) of the model (representing the median corner frequency over the population); η_{event} is the interevent residual distribution (i.e., event-specific adjustments to e_1); η_{duration}, $\eta_{\text{propagation}}$, and η_{site} denote the crossed random intercepts for the grouping levels duration, propagation, and site, respectively. Finally, ϵ is the leftover residual distribution. All together, η_{duration}, $\eta_{\text{propagation}}$, η_{site}, and ϵ describe the intra-event residuals (i.e., variability of $\log(f_c)$ within the set of results for any given earthquake). The random effects η_{duration}, $\eta_{\text{propagation}}$, and η_{site} are zero-mean normal distributions with standard deviations ϕ_{duration}, $\phi_{\text{propagation}}$, and ϕ_{site}, respectively. In the following, we consider the following standard deviations (Atik *et al.*, 2010):

$$\phi_{\text{dps}} = \sqrt{\phi^2_{\text{duration}} + \phi^2_{\text{propagation}} + \phi^2_{\text{site}}}, \quad (2a)$$

$$\phi = \sqrt{\phi^2_{\text{dps}} + \phi^2_0}, \quad (2b)$$

in which ϕ_0 is the standard deviation of the normal distribution ϵ.

Figure 5 shows the random intercepts of the three groups together with their errors. The random effects are positive for AVE and EPIH models in the site and propagation grouping levels, respectively, in agreement with the evidences shown by Figures 3 and 4. Regarding the duration grouping level, the random effect for 20 s is positive and larger than for 5 s. Looking at Figure 2, although events with f_c less than 3 Hz show a f_c for 20 s smaller than for 5 s, for most events with f_c greater than 3 Hz, a duration of 5 s yields slightly smaller f_c (the mean value of the ratio $f_c^{20\text{ s}}/f_c^{5\text{ s}}$ is about 0.2), in agreement with the random effect relative values.

Considering the 20 s window duration, EPIH attenuation, and SEL site constraint, the standard deviations ϕ_{duration}, $\phi_{\text{propagation}}$, and ϕ_{site} for $\log(f_c)$ are 0.01531, 0.03410, and

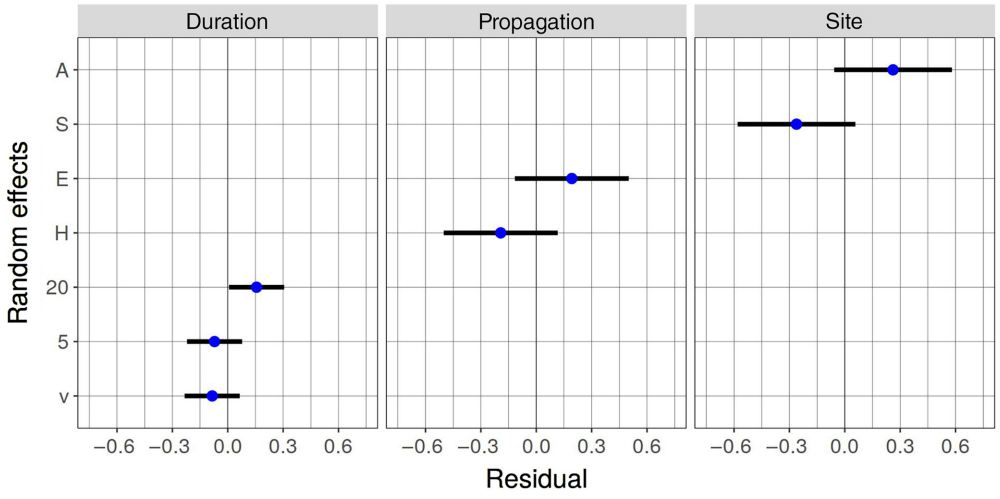

Figure 5. Random intercepts for the duration ($\eta_{duration}$), propagation ($\eta_{propagation}$), and site constraint (η_{site}) group factors (see equation 1). Random effects A, S, H, E, 20, 5, and v correspond to: AVE and SEL choices for the site group; HYPO and EPIH for the propagation group; 20 s, 5 s, and variable duration for the duration group. The color version of this figure is available only in the electronic edition.

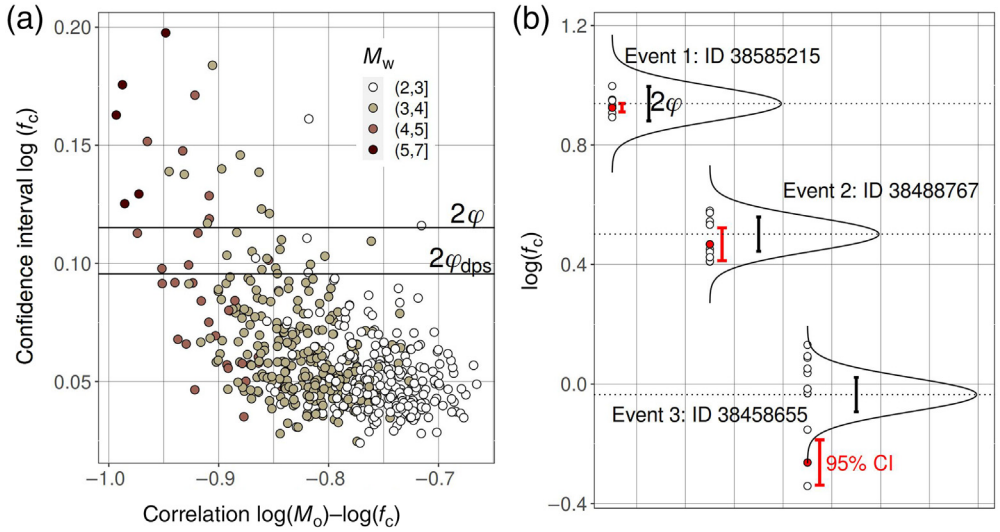

Figure 6. (a) 95% confidence intervals for log(f_c) computed considering 20 s duration, EPIH attenuation, and SEL site constraint. Correlation between source parameters is computed from the covariance matrix. Horizontal lines correspond to two times the intraevent standard deviations ϕ and ϕ_{dps} (see equations 2a and 2b). (b) log(f_c) obtained for three events. The circles indicate values obtained for the 12 branches of Figure 1; the filled circle indicates results for 20 s window duration, EPIH attenuation model, and SEL site constraint; the vertical bars close to the filled circle indicate 95% confidence interval for log(f_c). Gaussian distributions represent the intraevent residuals centered on the event-corrected intercept and standard deviation ϕ. The color version of this figure is available only in the electronic edition.

0.03708, respectively, whereas ϕ_0 is 0.0337. Thus, the largest contributions to the variability of residuals are made by the alternative choices for the attenuation model and for constraining the sites. The overall intraevent standard deviation is $\phi = 0.0625$; excluding the left-over residuals, the intraevent standard deviation becomes $\phi_{dps} = 0.0526$. In Figure 6a, the extension of the 95% CIs of log(f_c) is shown against the correlation between log(M_0) and log(f_c). If we consider ϕ as an estimate of epistemic uncertainty, Figure 6 shows that the extent of the 95% CIs is smaller than 2ϕ for most of the considered earthquakes, particularly for $M_w < 4$.

Figure 6b exemplifies the comparison between log(f_c) as estimated by the 12 branches of the logic tree (Fig. 1), the width of the 95% CI for a specific branch (i.e., 20 s window duration, EPIH and SEL), and a normal distribution centered on the event-adjusted intercept (i.e., combination of e_1 and η_{event} in equation 1) and with standard deviation equal to ϕ. For event 1 (magnitude 2.7), log(f_c) for the selected branch is within the range defined by the 12 branches, but the width of the 95% CI is much narrower than ϕ: for event 1, the estimated uncertainty of log(f_c) underestimates the model uncertainty. Also for event 2 (magnitude 3.3), log(f_c) is close to the mean over the 12 branches, but for this event the width of the 95% CI is comparable with 2ϕ. Event 3 (magnitude 4.2) represents the case when the width of the 95% CI is comparable with 2ϕ, but the estimated log(f_c) lies in the tail of the distribution of values for all branches.

The random intercepts shown in Figure 5 quantify the contribution of different model assumptions to the variability of source parameters. To visualize the impact that alternative assumptions have on the Fourier spectra, we prepare

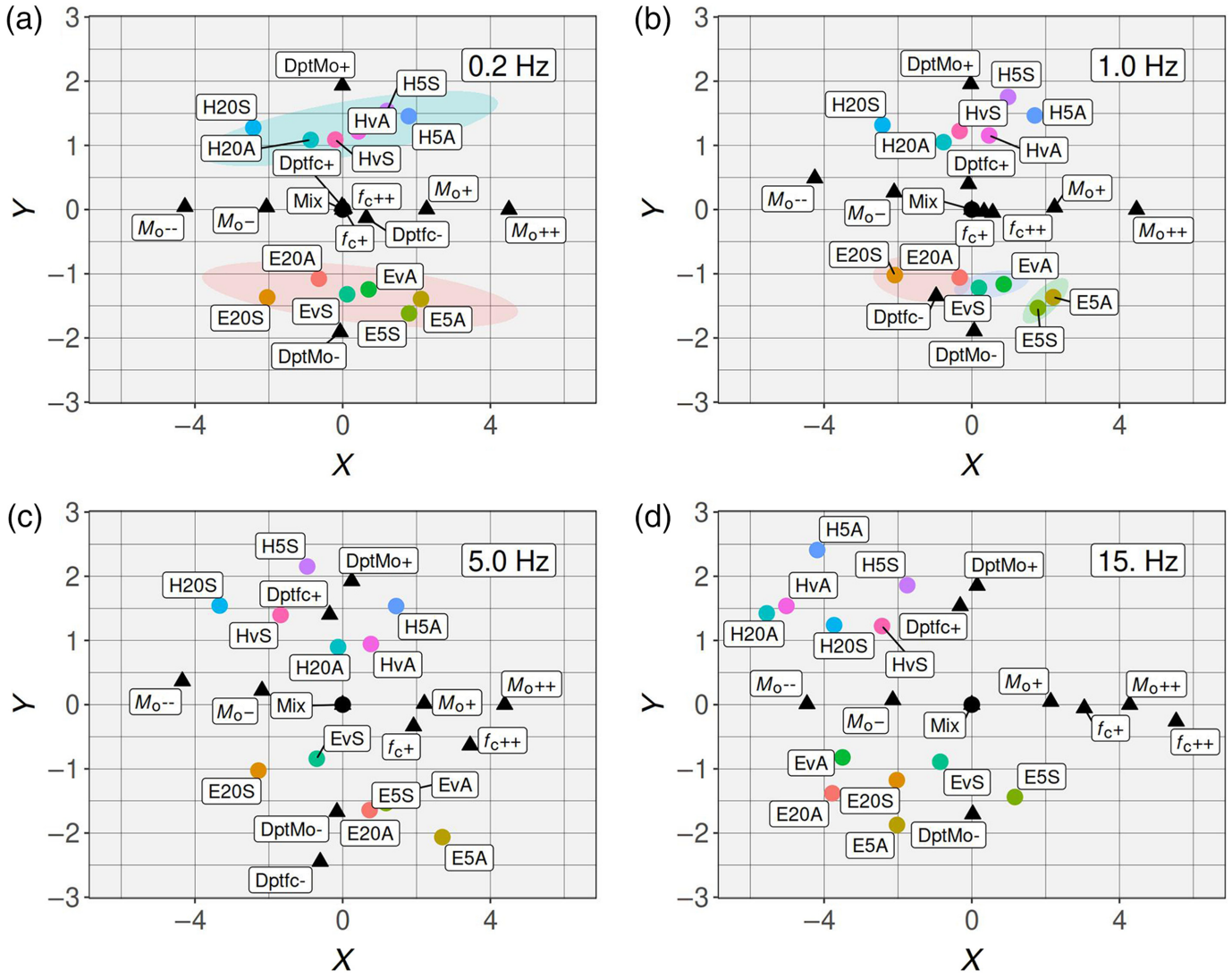

Figure 7. Sammon's maps showing the proximity of the Fourier spectral amplitudes computed for four frequencies (i.e., 0.2, 1.0, 5.0, and 25 Hz) considering the source parameters related to the 12 branches of the logic tree shown in Figure 1. Each model is identified by a label consisting of: attenuation model (E for EPIH and H for HYPO), duration (5, 20, v refer to 5 s, 20 s, and variable duration, respectively), site constraint (A stands for AVE and S for SEL). The triangles indicate synthetic models added as reference; Mix (in the center of the map) indicates the synthetic model that has the logarithm of the seismic moment and corner frequency equal to the average values computed over all 12 models. The color version of this figure is available only in the electronic edition.

Sammon maps (Sammon, 1969; Scherbaum *et al.*, 2010; Fig. 7). The multidimensional vector used as input for the Sammon map is computed by predicting the source spectra using the seismic moments and corner frequencies of 462 earthquakes common to all 12 branches of the logic tree. Spectral amplitudes are computed at 0.2, 1.0, 5.0, and 15 Hz using the source model adopted by each branch. To provide a reference point in Sammon's map, spectral amplitudes are also computed for the mean of the corner frequency and of the logarithm of the seismic moment, shown as Mix in Figure 7 (black dot).

In addition, because the X and Y axes defining the Sammon maps have no special significance, artificial models are constructed to facilitate interpretations (Bindi *et al.*, 2017). The artificial models denoted with M+ and M++ are obtained using the mean corner frequencies and adding 0.1 and 0.2 units to the mean LogM_0, respectively. Similarly, M− and M−− models are constructed subtracting 0.1 and 0.2 units from the mean LogM_0, respectively. Artificial models f + and f + + are constructed using the mean LogM_0 and multiplying the mean corner frequencies by 1.2 and 1.4, respectively. Finally, the artificial models DptM_0+ and DptM_0− are constructed by considering the mean corner frequencies and adding, or subtracting, the term $0.03\Delta h$ to the mean LogM_0, in which Δh is the difference between the depth of each event and the mean depth of the population. Models Dptf_c+ and Dptf_c− are constructed similarly, but considering the mean LogM_0 and perturbing the mean f_c of each event. Finally, the Sammon maps

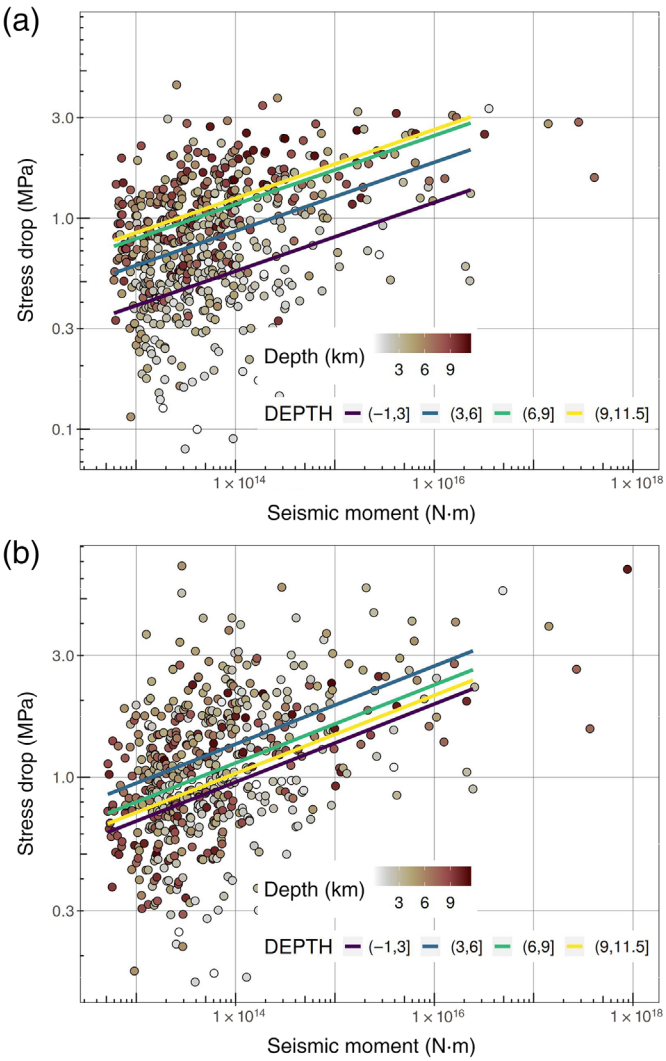

Figure 8. Scaling of stress drop with seismic moment considering the (a) HYPO and (b) EPIH attenuation models, 20 s window duration, and SEL site constraint. The lines show the slopes obtained for different depth intervals, considering random intercepts for the depth grouping factors (see equation 6). The color version of this figure is available only in the electronic edition.

are translated and rotated to center the origin of the coordinate system on the Mix model and to locate M++ along the positive x axis (Fig. 7). A reflection with respect to the x axis is also applied to orient the positive y axis direction toward DptM_0+. These transformations do not change the interpoint distances but facilitate the comparison of different maps.

The interpoint distances in Figure 7 are a measure of the closeness of the source spectral amplitudes predicted by the models associated with each branch of the logic tree. The most striking feature, which is persistent across all frequencies, is the separation between models using HYPO attenuation model from those using EPIH. At 0.2 Hz, the spectral amplitudes are controlled by the seismic moment, and differences on the corner frequencies do not play a role. Therefore, the *fc*+ and *fc*++ models are almost coincident with Mix. However, the different models do not spread along the M++ direction but in the DptM_0+ and DptM_0− directions. This is consistent with the fact that the treatment of depth dependencies is the main difference between HYPO and EPIH models. At 1.0 Hz, variability affecting f_c begins to play a role that becomes stronger at 5 Hz, in which the DptM_0+ and Dptf_c+ models are closely located and both identify the direction along which the different models spread (the same is also true for DptM_0− and Dpf_c−). At low frequencies (i.e., 0.2 and 1 Hz), models within the HYPO and EPIH groups tend to cluster according to window duration, whereas for high frequencies (i.e., 5 and 15 Hz), they cluster according to the site constraints.

Stress Drop

The stress-drop values are computed from seismic moment M_0 and source radius r as follows (Eshelby, 1957; Keilis-Borok, 1959):

$$\Delta\sigma = \frac{7}{16}\frac{M_0}{r^3}. \tag{3}$$

Assuming a circular crack model with uniform stress drop, the source radius can be computed from the corner frequency (Brune, 1970; Madariaga, 1976):

$$r = \frac{k\beta}{f_c}, \tag{4}$$

in which k = 0.37 (Brune, 1970, 1971). Regarding the shear-wave velocity β, following Bindi *et al.* (2021) we tested three different choices: a constant value β = 3200 m/s; velocities β extracted from a 1D regional velocity model (R. Graves, personal comm.) using linear interpolation; velocities β extracted from a regional 3D velocity model (White *et al.*, 2021) using bilinear interpolation (see Fig. S2).

The uncertainty on $\Delta\sigma$ is computed by propagating the errors from $\log M_0$ and f_c. Differently from previous studies (Fletcher *et al.*, 1984; Prieto *et al.*, 2007; Cotton *et al.*, 2013), we also consider the contribution from the correlation $\delta_{f_c,\log M_0}$ between $\log M_0$ and f_c as provided by the covariance matrix of the fit. In fact, Figure 6a shows that the negative correlation between the source parameters varies between −1 and −0.6. Considering a first-order Taylor approximation, the error propagated to $\Delta\sigma$ is (Bindi *et al.*, 2018):

$$\delta_{\Delta\sigma} = \Delta\sigma\sqrt{\left|9\left(\frac{\delta_{f_c}}{f_c}\right)^2 + [\ln(10)]^2\delta^2_{\log M_0} + \frac{6\ln(10)}{f_c}\delta_{f_c,\log M_0}\right|}. \tag{5}$$

Finally, we apply a random-effect regression (Bates *et al.*, 2015) to a linear model describing the dependency of $\log\Delta\sigma$ on $\log M_0$, considering depth-dependent random intercepts, that is

$$\log\Delta\sigma = b_1 + \alpha\log(M_0) + \Gamma_{D_k} + \varepsilon, \tag{6}$$

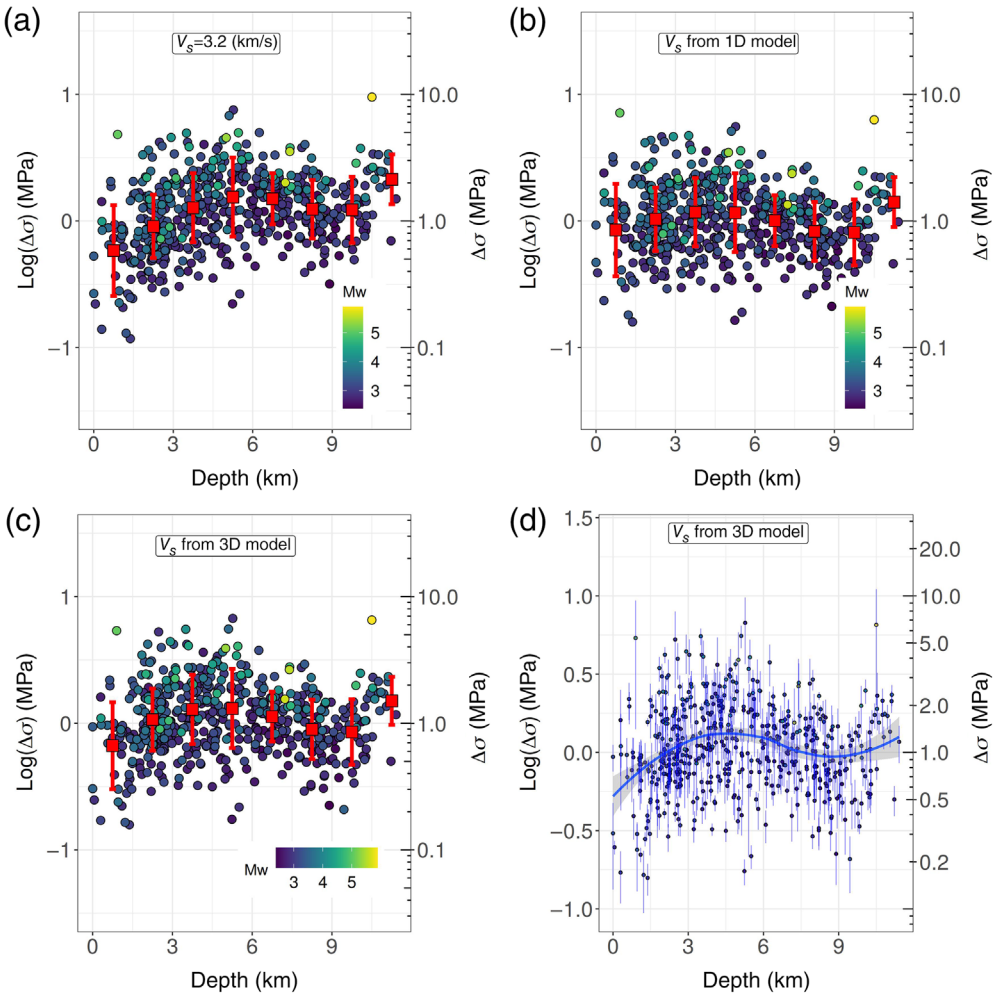

Figure 9. Scaling of stress drop $\Delta\sigma$ with hypocentral depth considering 20 s duration, EPIH attenuation, and SEL site constraints. (a) A constant shear-wave velocity $\beta = 3.2$ km/s is used to compute $\Delta\sigma$; (b) a regional 1D velocity model is considered (R. Graves, personal comm.); (c) a 3D velocity model is considered (White *et al.*, 2021). In panels (a–d), average $\Delta\sigma \pm$ one standard deviation values computed for depth intervals 1.5 km thick are shown as vertical bars. (d) $\Delta\sigma$ values of panel (c) are shown with their 95% confidence intervals; the trend line is based on localized regression. The color version of this figure is available only in the electronic edition.

in which the random effects Γ_{D_k} on the intercept b_1 are grouped by depth intervals considering four classes k = 1,...,4 that correspond to: <3, 3–6, 6–9, >9 km. Attempts considering also random slopes did not indicate any significant role of depth on determining α.

The average stress drop increases with event size for both the EPIH and HYPO attenuation models as shown in Figure 8. The slope α for the HYPO and EPIH models is 0.131 ± 0.015 and 0.153 ± 0.015, respectively. $\Delta\sigma$ varies over two orders of magnitude between 0.1 and 10 MPa with most of the values within the 0.3–3 MPa range. The random intercepts for HYPO show a clear depth dependence, with deep events having, on average, higher stress drops than shallow events, whereas for EPIH, the random intercepts do not scale with depth. Therefore, EPIH is absorbing depth-dependent effects, which are transferred to the source when HYPO is considered. Differences in $\Delta\sigma$ obtained considering EPIH and HYPO are shown in Figure S2B,C : for the deepest events, the ratio is lower than 0.5.

The impact of the selected velocity model on $\Delta\sigma$ is shown in Figure 9 for EPIH. If a constant velocity is used (Fig. 9a), $\Delta\sigma$ shows an increasing trend from surface to 5 km and for depths deeper than 9 km. Because the shear-wave velocity increases with depth, in particular in the uppermost 6 km (Fig. S3), the $\Delta\sigma$ trends can be partially explained by velocity variations. Indeed, when a 1D (Fig. 9b) or a 3D (Fig. 9c) velocity model is considered, $\Delta\sigma$ show no systematic trend in the depth range analyzed.

Discussion

Determining source parameters is hampered by tradeoffs involving source, propagation, and site terms, and restoring uniqueness of solution requires assumptions that differ from study to study (Shearer *et al.*, 2019). In addition, the limited bandwidth available for analysis reduces the ability to discriminate source effects from propagation effects and it increases the correlation between source parameters (Abercrombie, 2021). Several benchmark studies have been performed to evaluate the impact of processing and model assumptions on source parameter uncertainties by comparing the results of different techniques applied to the same data set (e.g., Shearer *et al.*, 2019; Pennington *et al.*, 2021; Morasca *et al.*, 2022; Shible *et al.*, 2022). In this work, we focused on one specific approach called GIT that we applied to the data set compiled for a community stress-drop validation study (Baltay *et al.*, 2021), consisting of records from the Ridgecrest 2019 sequence. We investigated two different uncertainties: the precision of the source parameters (i.e., seismic moment and corner frequency) obtained from a spectral fit, and the epistemic uncertainties related to model assumptions. In the companion article (see Data and Resources), we compared the precision of the source parameters by considering approaches based on asymptotic

errors, on Monte Carlo sampling, and on model comparison. Because the different approaches generate consistent estimates, here we consider CIs based on asymptotic standard errors because they require less computational effort.

The length of the 95% CI of $\log(f_c)$ (Fig. 6a) shows a large scatter and, for magnitudes smaller than about 3, they vary around 0.05. For larger magnitudes, 95% CI shows a tendency to increase and, for magnitudes above 5, it definitely exceeds 0.1. These values suggest that the precision deteriorates when the corner frequencies approach the lower end of the available bandwidth. This is a consequence of the inverse correlation between $\mathrm{Log}M_0$ and f_c because the spectral values above the corner are controlled by the product $M_0 f_c^2$. When compared with the intraevent variability ϕ (defined in equation 3), Figure 6 shows that the precision may underestimate the overall uncertainty of the source parameters (e.g., event 1 in Fig. 6b) because it does not account for a significant epistemic contribution associated with assumptions in data processing (e.g., the duration of the analyzed windows), in the decomposition (e.g., description of the depth dependency of attenuation), and in the interpretation of the results (e.g., the source models used for the fit), among others not investigated in this study. It is also worth noting that although the uncertainty of the results of a specific branch might be comparable to the spread associated with multiple branches, the mean value of the branch might be biased against the population mean (e.g., event 3 in Fig. 6b). Therefore, the comparison of results obtained by applying different techniques to the same data set, or making different assumptions for the same technique, can help in assessing the impact of the model assumptions. We organized the different choices in a logic-tree framework (Fig. 1), and we quantified in terms of random intercepts (Fig. 5) the systematic contribution to the intraevent variability by alternative choices operated at the branching levels. Sammon's maps (Fig. 7) show that the predicted source spectra cluster according to the attenuation model used (i.e., HYPO or EPIH) at all frequencies. Within the two attenuation clusters, the source spectra group, at high frequencies, according to the used site amplification constraint. Therefore, not only do different assumptions generate systematic deviations from the population median that contribute to intraevent variability, but also they can lead to different interpretation of the results as shown in Figure 8. In this figure, the stress drop $\Delta\sigma$ is shown against seismic moment M_0. Considering the linear model in equation (7), $\log(\Delta\sigma)$ shows a linear increase with $\log(M_0)$. The difference is in the depth dependency of the intercept: when the hypocentral attenuation model (HYPO) is considered (Fig. 8a), the intercept scales with the hypocentral depth (i.e., the average $\Delta\sigma$ increases with depth), whereas using the EPIH attenuation model, average depth dependencies of $\Delta\sigma$ are partially absorbed by the attenuation (Fig. 8b). Although weaker than for the HYPO attenuation model, the $\Delta\sigma$ values obtained considering the EPIH attenuation model still show depth dependencies (Fig. 9), in particular between surface and 5 km and for events deeper than 9 km. Anyway, the strength of the dependency depends on the shear-wave velocity model considered as shown in Figure 9, in which the $\Delta\sigma$ trends with depth are compared for three difference choices: the trend developing in particular at shallow depths is weakened when the increase in velocity with depth is accounted for through 1D or 3D models. Therefore, the existence of trends indicating an increase in $\Delta\sigma$ with depth depends on both the attenuation model implemented to perform the decomposition and the shear-wave velocity considered to calculate $\Delta\sigma$. Consequently, whether the observed trend with depth is apparent and due to model assumptions is difficult to resolve and still a matter of debate (Abercrombie *et al.*, 2021; Pennington *et al.*, 2021).

Conclusions

In this work, and in the companion article (see Data and Resources), we investigated the uncertainties of seismic moment and corner frequency estimated for earthquakes selected within the data set compiled for a community stress-drop validation study (Baltay *et al.*, 2021), consisting of records from the Ridgecrest 2019 sequence (southern California).

1. The decomposition approach applied to isolate source spectra from propagation and site effects requires a priori assumptions to restore the uniqueness of the solution; consequently, comparison of the results obtained with alternative choices (i.e., following a logic-tree approach) can help identify systematic biases and provide an estimate of the epistemic uncertainty;
2. among the analyzed processing and model assumptions, the choice about the propagation model has a strong impact on the results and their interpretation; in terms of corner frequencies, the attenuation model accounting explicitly for depth dependencies (EPIH) generates corner frequencies for events shallower than 6 km on average 10% larger than the model using the hypocentral distance (HYPO); regarding the duration of *S* wave window selected to compute the Fourier spectra, the ratio of f_c estimates for a duration of 20 s to those for 5 s decreases with increasing magnitude, with the average ratio decreasing from 1.1 for $M_w < 3$ to 0.66 for $M_w > 4.5$;
3. treating the processing and model assumptions as random effects, the standard deviation ϕ of the intraevent residuals for $\log(f_c)$ is 0.0635, corresponding to a corner frequency ratio $10^{2\phi} = 1.33$; the extent of the 95% CI of $\log(f_c)$ is generally less than 2ϕ, suggesting that the uncertainty provided for the source parameters might underestimate the model-related uncertainty (epistemic uncertainty);
4. the 95% CI of $\log(f_c)$ varies around 0.05 for magnitudes smaller than 3; for larger events, it increases in accordance with the increase in the inverse correlation between corner frequency and seismic moment because of the limited bandwidth available; and

5. the computed stress drop $\Delta\sigma$ varies mostly between 0.1 and 10 MPa, and a linear increase in $\Delta\sigma$ with $\log(M_0)$ is observed regardless of the model assumptions; conversely, the existence of trends indicating an increase in $\Delta\sigma$ with depth depends on both the attenuation model and the shear wave velocity considered: no significant trend is detected when depth-dependent attenuation and velocities are used.

In summary, because high-quality data from a modern dense network allow source parameters of small and moderate events to be calculated with small uncertainty (high precision), an assessment of processing- and model-related uncertainties becomes important to uncover systematic bias, to provide an estimate of epistemic uncertainty, and to support the interpretation of the final results.

Data and Resources

This study has been performed within the framework of the community stress-drop validation study (Baltay *et al.*, 2021) organized as Southern California Earthquake Center (SCEC) Technical Activity Group. Waveforms and metadata is available at https://www.scec.org/research/stress-drop-validation (last accessed December 2022). Analyses have been performed in R (R Core Team, 2020) using packages ggplot2 (Wickham, 2016), lme4 (Bates *et al.*, 2015), scico (Pedersen and Crameri, 2021), viridis (Garnier *et al.*, 2021), and MASS (Venables and Ripley, 2002). This study is the second of two companion studies: the results of the first study (Bindi *et al.*, 2023b) are available at Bindi *et al.* (2023a). The supplemental material includes Figures S1–S3: Figure S1 showing the ratio of the corner frequencies obtained considering different window duration against magnitude; Figure S2 shows stress-drop values obtained considering different window duration and attenuation models; and Figure S3 compares the shear-wave velocities at the hypocentral locations, considering 1D and 3D regional velocity models.

Declaration of Competing Interests

The authors acknowledge that there are no conflicts of interest recorded.

Acknowledgments

The authors thank R. Abercrombie, A. Baltay, and Taka'aki Taira for organizing and managing the community stress-drop validation study. Thanks are also due to two anonymous reviewers and the Associate Editor for their useful suggestions. This research has been financially supported by the European Plate Observing System (EPOS) Research Infrastructure through the contribution of the Italian Ministry of University and Research (MUR)—EPOS ITALIA Joint Research Unit.

References

Abercrombie, R. E. (2021). Resolution and uncertainties in estimates of earthquake stress drop and energy release, *Phil. Trans. Roy. Soc. Lond. A* **379,** no. 2196, doi: 10.1098/rsta.2020.0131.

Abercrombie, R. E., D. T. Trugman, P. M. Shearer, X. Chen, J. Zhang, C. N. Pennington, J. L. Hardebeck, T. H. W. Goebel, and C. J. Ruhl (2021). Does earthquake stress drop increase with depth in the crust? *J. Geophys. Res.* **126,** no. 10, e2021JB022314, doi: 10.1029/2021JB022314.

Andrews, D. J. (1986). Objective determination of source parameters and similarity of earthquakes of different size, *American Geophysical Union (AGU)*, 259–267.

Atik, L. A., N. Abrahamson, J. J. Bommer, F. Scherbaum, F. Cotton, and N. Kuehn (2010). The variability of ground-motion prediction models and its components, *Seismol. Res. Lett.* **81,** no. 5, 794–801.

Baltay, A., R. Abercrombie, and T. Taira (2021). A community stress drop validation study using the 2019 Ridgecrest earthquake dataset, *SSA Annual Meeting*, virtual meeting, 19–23 April 2021, available at https://www.seismosoc.org/annual-meeting/2021program/ (last accessed May 2023).

Bates, D., M. Mächler, B. Bolker, and S. Walker (2015). Fitting linear mixed-effects models using lme4, *J. Stat. Software* **67,** no. 1, 1–48.

Bindi, D., F. Cotton, S. R. Kotha, C. Bosse, D. Stromeyer, and G. Grünthal (2017). Application-driven ground motion prediction equation for seismic hazard assessments in non-cratonic moderate-seismicity areas, *J. Seismol.* **21,** 1201–1218.

Bindi, D., F. Cotton, D. Spallarossa, M. Picozzi, and E. Rivalta (2018). Temporal variability of ground shaking and stress drop in central Italy: A hint for fault healing? *Bull. Seismol. Soc. Am.* **108,** no. 4, 1853–1863.

Bindi, D., H. N. T. Razafindrakoto, M. Picozzi, and A. Oth (2021). Stress drop derived from spectral analysis considering the hypocentral depth in the attenuation model: Application to the Ridgecrest region, California, *Bull. Seismol. Soc. Am.* **111,** no. 6, 3175–3188.

Bindi, D., D. Spallarossa, M. Picozzi, and P. Morasca (2020). Reliability of source parameters for small events in central Italy: Insights from spectral decomposition analysis applied to both synthetic and real data, *Bull. Seismol. Soc. Am.* **110,** no. 6, 3139–3157.

Bindi, D., D. Spallarossa, M. Picozzi, A. Oth, P. Morasca, and K. Mayeda (2023a). Spectral decomposition results for the SCEC-community stress drop validation study, *GFZ Data Services* doi: 10.5880/GFZ.2.6.2023.005.

Bindi, D., D. Spallarossa, M. Picozzi, A. Oth, P. Morasca, and K. Mayeda (2023b). The community stress-drop validation study—Part I: Source, propagation, and site decomposition of Fourier spectra, *Seismol. Res. Lett.* doi: 10.1785/0220230019

Brune, J. N. (1970). Tectonic stress and the spectra of seismic shear waves from earthquakes, *J. Geophys. Res.* **75,** no. 26, 4997–5009.

Brune, J. N. (1971). Correction to "tectonic stress and the spectra, of seismic shear waves from earthquakes", *J. Geophys. Res.* **76,** no. 20, 5002–5002.

Chen, X., and R. E. Abercrombie (2020). Improved approach for stress drop estimation and its application to an induced earthquake sequence in Oklahoma, *Geophys. J. Int.* **223,** no. 1, 233–253.

Cotton, F., R. Archuleta, and M. Causse (2013). What is sigma of the stress drop? *Seismol. Res. Lett.* **84,** no. 1, 42–48.

Eshelby, J. D. (1957). The determination of the elastic field of an ellipsoidal inclusion, and related problems, *Proc. Math. Phys. Sci.* **241,** no. 1226, 376–396.

Fletcher, J., J. Boatwright, L. Haar, T. Hanks, and A. McGarr (1984). Source parameters for aftershocks of the Oroville, California, earthquake, *Bull. Seismol. Soc. Am.* **74,** no. 4, 1101–1123.

Garnier, S., N. Ross, R. Rudis, A. P. Camargo, M. Sciaini, and C. Scherer (2021). viridis: Colorblind-friendly color maps for R, *R package version 0.6.2*.

Keilis-Borok, V. (1959). On estimation of the displacement in an earthquake source and of source dimensions, *Ann. Geophys.* **12,** no. 2, 205–214.

Madariaga, R. (1976). Dynamics of an expanding circular fault, *Bull. Seismol. Soc. Am.* **66,** no. 3, 639–666.

Morasca, P., D. Bindi, K. Mayeda, J. Roman-Nieves, J. Barno, W. R. Walter, and D. Spallarossa (2022). Source scaling comparison and validation in central Italy: Data intensive direct s waves versus the sparse data coda envelope methodology, *Geophys. J. Int.* **231,** 1573–1590.

Pedersen, T. L., and F. Crameri (2021). scico: Colour palettes based on the scientific colour-maps, *R package version 1.3.0*.

Pennington, C. N., X. Chen, R. E. Abercrombie, and Q. Wu (2021). Cross validation of stress drop estimates and interpretations for the 2011 Prague, ok, earthquake sequence using multiple methods, *J. Geophys. Res.* **126,** no. 3, e2020JB020888 , doi: 10.1029/2020JB020888.

Prieto, G. A., D. J. Thomson, F. L. Vernon, P. M. Shearer, and R. L. Parker (2007). Confidence intervals for earthquake source parameters, *Geophys. J. Int.* **168,** no. 3, 1227–1234.

R Core Team (2020). *R: A language and environment for statistical computing*, R Foundation for Statistical Computing, Vienna, Austria.

Sammon, J. (1969). A nonlinear mapping for data structure analysis, *IEEE Trans. Comput.* **18,** no. 5, 401–409.

Scherbaum, F., N. M. Kuehn, M. Ohrnberger, and A. Koehler (2010). Exploring the proximity of ground-motion models using high-dimensional visualization techniques, *Earthq. Spectra* **26,** no. 4, 1117–1138.

Shearer, P. M., R. E. Abercrombie, D. T. Trugman, and W. Wang (2019). Comparing egf methods for estimating corner frequency and stress drop from p wave spectra, *J. Geophys. Res.* **124,** no. 4, 3966–3986.

Shible, H., F. Hollender, D. Bindi, P. Traversa, A. Oth, B. Edwards, P. Klin, H. Kawase, I. Grendas, R. R. Castro, *et al.* (2022). GITEC: A generalized inversion technique benchmark, *Bull. Seismol. Soc. Am.* **112,** no. 2, 850–877.

Stafford, P. J. (2014). Crossed and nested mixed–effects approaches for enhanced model development and removal of the ergodic assumption in empirical ground–motion models, *Bull. Seismol. Soc. Am.* **104,** no. 2, 702–719.

Venables, W. N., and B. D. Ripley (2002). *Modern Applied Statistics With S*, Fourth Ed., Springer, New York.

White, M. C. A., H. Fang, R. D. Catchings, M. R. Goldman, J. H. Steidl, and Y. Ben-Zion (2021). Detailed traveltime tomography and seismic catalogue around the 2019 Mw7.1 Ridgecrest, California, earthquake using dense rapid-response seismic data, *Geophys. J. Int.* **227,** no. 1, 204–227.

Wickham, H. (2016). *ggplot2: Elegant Graphics for Data Analysis*, Springer-Verlag, New York.

Manuscript received 27 January 2023
Published online 23 May 2023